Cement and Concrete Composites 143 (2023) 105276

Contents lists available at ScienceDirect

Cement and Concrete Composites

journal homepage: www.elsevier.com/locate/cemconcomp

Morphological, microstructural, and mechanical properties of highly-ordered C–S–H regulated by cellulose nanocrystals (CNCs)

Yuhuan Wang [a], Sarah Goodman [b], Yi Bao [a], Weina Meng [a,*]

[a] Department of Civil, Environmental and Ocean Engineering, Stevens Institute of Technology, Hoboken, NJ, 07030, USA
[b] Department of Chemical Engineering and Materials Science, Stevens Institute of Technology, Hoboken, NJ, 07030, USA

ARTICLE INFO

Keywords:
Nanocomposites
Calcium silicate hydrates (C–S–H)
Cellulose nanocrystals (CNCs)
Mechanical property
Microstructure
Morphology

ABSTRACT

Microstructures of calcium silicate hydrates (C–S–H) are relevant to the mechanical properties and durability of cement-based materials. Random growth of the microstructures of C–S–H largely compromises the mechanical properties and durability. This paper proposes to utilize cellulose nanocrystals (CNCs) to modify the microstructures of C–S–H. This research investigates the effect of CNCs on the morphological, microstructural, and mechanical properties of C–S–H through dynamic light scattering (DLS), transmission electron microscopy (TEM), scanning electron microscopy (SEM), Fourier transform infrared spectroscopy (FTIR), X-ray diffraction (XRD), thermogravimetry analysis (TGA), atomic force microscopy (AFM), and three-point bending tests. The results showed that CNCs effectively mitigated the agglomeration of C–S–H and generated C–S–H/CNC nanocomposites with highly ordered, layered, and dense microstructures. The C–S–H and CNCs in the C–S–H/CNC nanocomposites had strong interactions through hydrogen bonds and calcium ion coordination bonds. The strong interactions and ordered microstructures enable C–S–H/CNCs nanocomposites to achieve high strength and flexibility.

1. Introduction

Calcium silicate hydrates (C–S–H) are important hydration products of Portland cement [1]. The microstructures of C–S–H play critical roles in the mechanical properties and durability of cement-based materials such as concrete. In concrete, C–S–H is produced as nanoparticles during cement hydration. C–S–H nanoparticles tend to agglomerate and precipitate rapidly as gel-like aggregates with spatially-disordered porous microstructures [2]. Such microstructures adversely impact the physicochemical and mechanical properties as well as the durability of concrete [3–5]. Refining the microstructure of C–S–H is beneficial for the improvement of the mechanical properties and durability of cement-based materials [6,7].

Two important strategies have been developed to refine the microstructures of C–S–H. The first strategy is to use polymeric dispersants to modify the microstructures of C–S–H via hindering the agglomeration of C–S–H through surface adsorption or interlayer intercalation of polymeric dispersants to C–S–H nanoparticles, as illustrated in Fig. 1(a) and Fig. 1(b) [6–10]. Example dispersants often used in concrete include styrene-butadiene rubber [2], polycarboxylate (PCE) [8–15], polyethylene glycol [16–18], polydimethylsiloxane [19,20], and poly(vinyl alcohol) (PVA) [21–23]. For example, on one hand, PVA chains can be intercalated into the interlayer of C–S–H particles which can lower the bulk modulus of C–S–H. On the other hand, some PVA chains absorbed on the surface of C–S–H to decrease the porosity of C–S–H [21]. PCE has been used to mitigate the agglomeration of C–S–H nanoparticles via adsorbing on the surface of C–S–H nanoparticles to provide the steric effect [8–15]. However, the addition of PCE results in an undesirable retardation on cement hydration since the polymer adsorption slows the dissolution of unhydrated cement particles, as shown in Fig. 1(c) [24,25].

The second strategy is to use nanomaterials as fine seeds to refine the microstructures of C–S–H through promoting chemical reactions [26,27]. Various nanomaterials have been used in prior research, such as carbon nanofibers [28–30], carbon nanotubes [31,32], graphene nanoplatelets [26,33,34], nano graphene oxide [35–37], nano silica [38,39], nano titania [40,41], and nano calcium carbonate [42,43] to promote cement hydration. For example, graphene oxide surfaces with oxygen functional groups are believed to optimize the microstructures of C–S–H through promoting nucleation and reducing the total porosity, as shown in Fig. 1(d) [44,45]. Carbon nanofibers or multi-walled carbon nanotubes can also act as a bridge between C–S–H which reduces cracks and

* Corresponding author.
E-mail address: wmeng3@stevens.edu (W. Meng).

https://doi.org/10.1016/j.cemconcomp.2023.105276
Received 11 April 2023; Received in revised form 14 July 2023; Accepted 30 August 2023
Available online 1 September 2023

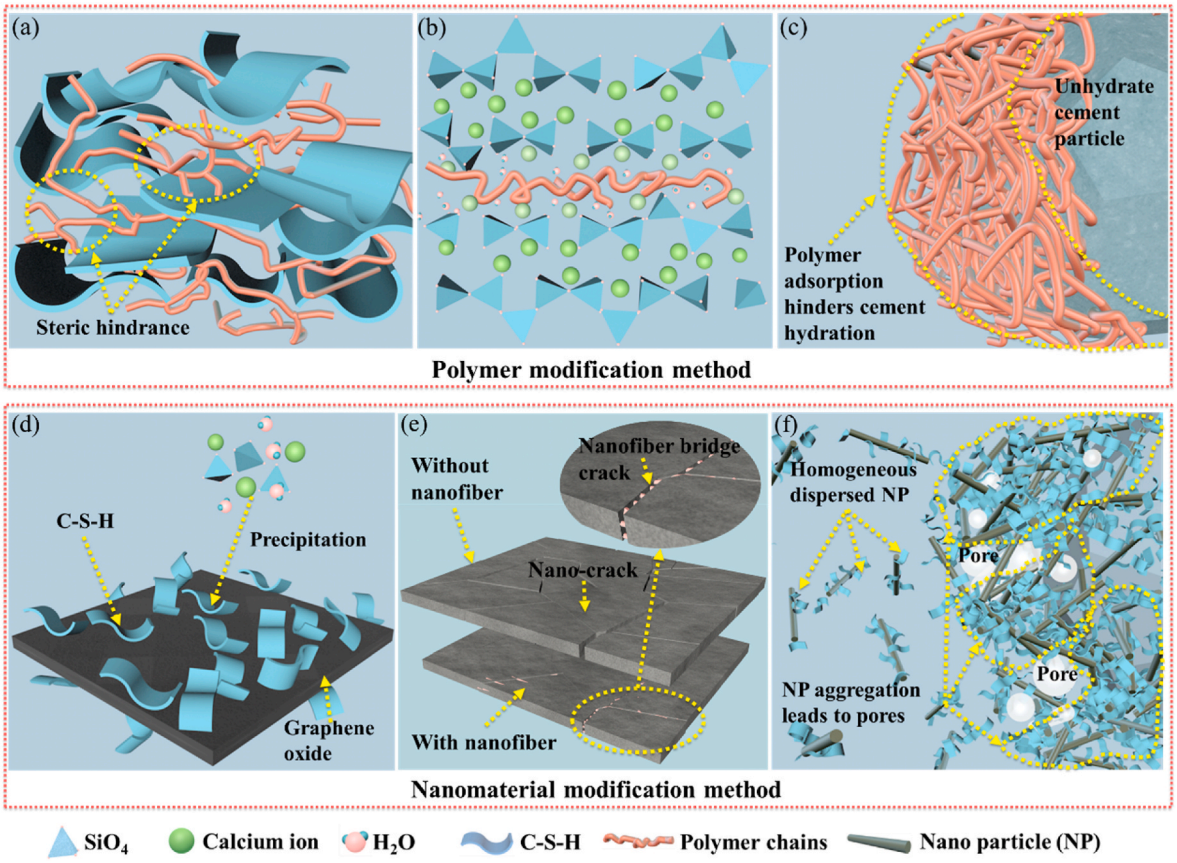

Fig. 1. Illustration of the two main strategies used to refine the microstructure of C–S–H: (a) polymer adsorption; (b) polymer intercalation; (c) polymer adsorption retards the hydration process of cement particle; (d) nanomaterials promote chemical reactions; (e) nanomaterials bridge cracks; (d) nanomaterial aggregation results in undesirable pores.

reduces the porosity of C–S–H by filling the pores, as shown in Fig. 1(e) [46]. It was reported that the addition of nano silica, nano titania, and carbon nanotubes to cement pastes increased the mean silicate chain length of C–S–H via the nucleation effect and the reduction of the interlayer water of C–S–H [47]. The use of nano silica also imparts the pozzolanic effect [47], which further densifies the microstructures of C–S–H via secondary hydration reactions in a long term. However, a recent study argued that carbon nanotubes do not provide nucleation sites for cement hydration [48]. Further research is necessary to achieve a consensus on the effects of carbon nanomaterials on the microstructures of C–S–H.

In addition to separately utilizing polymeric dispersants and nanomaterials to refine the microstructures of C–S–H, the two strategies have also been used synergistically. The combined use of polymeric dispersants and nanomaterials generated C–S–H-based nanocomposites with high mechanical properties [49]. Despite the exciting advances, C–S–H prepared through this method exhibits random porous microstructures [50,51]. Regulating the microstructures through polymers and/or nanomaterials is prohibited by their poor water dispersity, chemical inertness, and low agglomeration resistance. Some carbon nanomaterials such as carbon nanotubes need surface modification to increase the interfacial interaction with C–S–H [52,53]. As the nanomaterial dosage increased, agglomeration occurred [54–57], generating random porous microstructures, as shown in Fig. 1(f). In addition, most of the widely used polymers and nanomaterials are petroleum-based and have high carbon emission which in turn increases the carbon emission of concrete.

To address these challenges, this research proposes to incorporate cellulose nanocrystals (CNCs) into C–S–H system to improve its microstructures. This study is motivated by the various unique features of CNCs, which are a family of natural, renewable nanomaterials [58–60]. As shown in Fig. 2(a), with abundant hydroxy functional groups on the surface, CNCs exhibit desired water dispersity and aqueous stability, making CNCs promising materials that can be adsorbed on the surfaces of C–S–H and can provide steric repulsion to help disperse C–S–H nanoparticles [61]. Additionally, CNCs have lower costs and lower carbon emission than carbon nanofibers and carbon nanotubes [45–48]. CNCs also exhibit larger surface areas (100-1,300 m^2/g), higher aspect ratios (10–80), higher elastic modulus (140 GPa), higher tensile strength (7–10 GPa), and lower density (1.6 g/cm^3), making CNCs promising candidates to promote cement hydration [58,59,62].

Previous studies showed that adding CNCs into concrete influenced the fresh and hardened properties of concrete [63–65]. For example, CNCs were mixed with cement paste to reduce the viscosity at low dosages (<0.2%) of CNCs [61,66,67] and increase the viscosity at high dosages (>0.5%) [66]. Incorporating CNCs in concrete increased the mechanical properties of cement paste and concrete [43–46]. For instance, adding CNCs (0.2% by the volume of cement) increased the flexural strength of a cement paste by 20%, because CNCs promoted cement hydration by providing steric stabilization to disperse cement particles and by facilitating the transport of water from pore water to the unhydrated cement cores, as shown in Fig. 2(b) and (c) [61]. Both CNCs and PCE can disperse cement particles via steric stabilization, but CNCs can further promote cement hydration due to their high surface area. In addition, CNCs increased the volume fraction of high-density C–S–H and decreased the volume fraction of low-density C–S–H, which means that the CNCs may have the potential to modify the microstructures of cement hydration products [68]. CNCs promoted the formation of C–S–H in concrete under low temperature and low humidity conditions [69]. Recently, the effects of CNCs on the hydration of C_3S and the

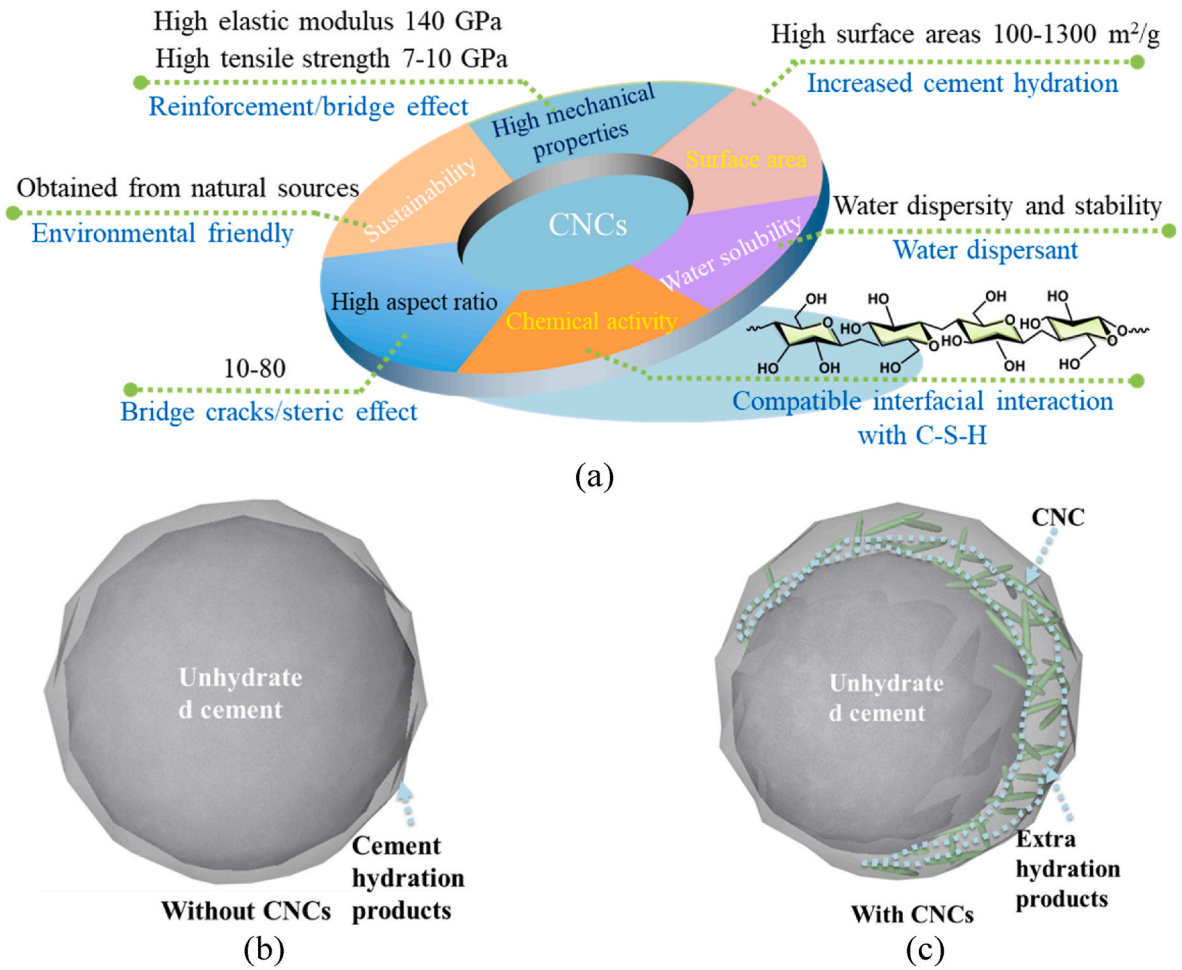

Fig. 2. Relevant characteristics and utilization of CNCs in cement-based systems: (a) the characteristics of CNCs; (b) the cement hydration process without CNCs; and (c) the mechanisms of CNCs promoting cement hydration.

nucleation effects of CNCs on the generation and polymerization degree of C–S–H were investigated [70]. It was found that CNCs helped promote the hydration of C_3S as well as the generation and polymerization degree of C–S–H, similar to many other nanomaterials with filler and seeding effects. Despite the above progress, the underlying mechanisms of the effects of CNCs on the morphology, microstructures, and mechanical properties of C–S–H remain unclear. Most of existing studies have mainly focused on bulk concrete properties evaluated through tests on a macro scale. The development of the microstructures of C–S–H in the presence of CNCs is unclear.

To address these fundamental knowledge gaps, this research aims to understand the effects of CNCs on the morphological, microstructural, and mechanical properties of C–S–H through comprehensive characterization techniques, including dynamic light scattering (DLS), transmission electron microscopy (TEM), polarization optical microscopy (POM), scanning electron microscopy (SEM), Fourier transform infrared

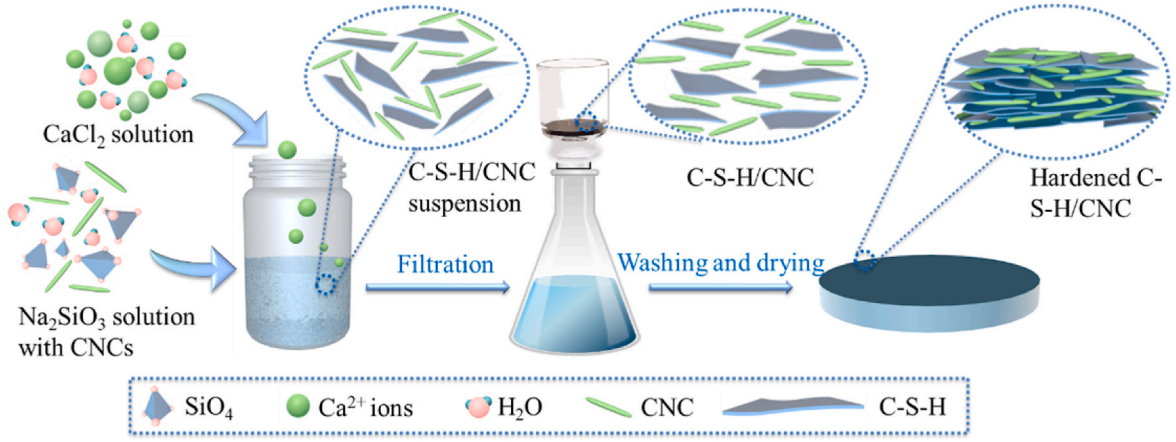

Fig. 3. Synthesis process of C–S–H/CNC colloidal suspensions and hardened C–S–H/CNC.

spectroscopy (FTIR), X-ray diffraction (XRD), thermogravimetry analysis (TGA), atomic force microscopy (AFM), and three-point bending tests. This research delivers new knowledge to support the development of advanced low-carbon cement-based materials with high mechanical properties, low carbon footprint, and excellent durability.

2. Experimental methods

2.1. Raw materials

In this research, calcium chloride ($CaCl_2$, 1 mol/L), sodium hydroxide (NaOH, 1 mol/L), and sodium metasilicate (Na_2SiO_3) were obtained from Fisher Scientific; CNCs were obtained from CelluForce; and sodium hydroxide (NaOH, 1 mol/L) was obtained from Innovating Science.

2.2. Synthesis of C–S–H and C–S–H/CNC

C–S–H suspensions were synthesized using a co-precipitation method [9,49,71], as shown in Fig. 3. In a typical synthetic run, $CaCl_2$ solution (30 mmol/L, obtained via diluting 1 mol/L $CaCl_2$) was added dropwise at a rate of 0.36 mL/min into Na_2SiO_3 solution (30 mmol/L) under magnetic stirring. After the addition of $CaCl_2$, the mixture was stirred for 12 h to ensure all reactive elements in the mixture precipitated. Then, DLS and TEM measurements were performed using the C–S–H suspensions. The initial pH value of the C–S–H suspensions was 11.2.

C–S–H/CNC suspensions were synthesized using a similar method. First, CNCs powder were dispersed in water using an ultrasonication disperser (model: IKA T 18 ULTRA-TURRAX Digital Disperser) to obtain a well dispersed CNC suspension with a concentration of 2% by mass. Next, the suspension was mixed with Na_2SiO_3 according to designed concentrations, which are 1 g/L, 3 g/L, 5 g/L, and 7 g/L. Then, $CaCl_2$ solution (30 mmol/L) was added into the mixture gradually. The mixture was stirred for 12 h to ensure all the reactive elements in the solution precipitated. The Ca/Si ratio was made equal to one by adjusting the concentrations of $CaCl_2$ and Na_2SiO_3. This Ca/Si ratio is consistent with references [9,71]. The pH of the system was adjusted to 11.2 via NaOH (1 mol/L), consistent with the pH of the C–S–H suspensions without CNCs. All solutions were stored in a glove box filled with nitrogen, and deionized water was boiled before the synthesis.

Hardened C–S–H and C–S–H/CNC samples were prepared by precipitating the C–S–H and C–S–H/CNC in suspensions via vacuum filtration [72] (47 mm in diameter with 0.2 μm in pore size), as shown in Fig. 3. The materials were washed using CO_2-free deionized water five times, and then they were vacuum dried and peeled from the filter. Five samples with different concentrations of CNCs (0 g/L, 1 g/L, 3 g/L, 5 g/L, and 7 g/L) were prepared and designated as C–S–H, C–S–H/CNC-1, C–S–H/CNC-3, C–S–H/CNC-5, and C–S–H/CNC-7, respectively.

2.3. Dynamic light scattering

Dynamic light scattering tests were performed to evaluate the stability of the CNCs, C–S–H, and C–S–H/CNC suspensions using a DLS analyzer (model: Zetasizer Nano ZS90 from Malvern Instruments Ltd., Malvern, UK). The stability of the suspensions was characterized by their zeta-potential and hydrodynamic diameters. The hydrodynamic diameter (also called dynamic diameter) is defined as the particle size obtained in aquatic environments [73]. In each measurement, the zeta-potential and dynamic diameters were measured three times at 25 °C, and the average value was calculated. For the preparation of samples, the CNCs were first dispersed in deionized water at a concentration of 0.1 g/L and then homogenized via bath sonication for 15 min before test. The C–S–H and the C–S–H/CNC suspensions synthesized before and after 6 months were used at the same concentration as the CNC suspension.

2.4. Transmission electron microscopy

The dispersion and the morphology of CNCs, C–S–H, and C–S–H/CNC were evaluated through transmission electron microscopy (TEM, model: JEOL 2100 Plus 200 keV). The samples for TEM examination were first sonicated 10 min and then prepared by dispersing the CNCs, C–S–H, and C–S–H/CNC suspensions at the same concentration (0.1 g/L) on a carbon-coated copper grid (etching 30 s before use). The CNC sample was stained with uranyl acetate. Filter paper was used to remove excessive liquid from the grid. The samples were air-dried for 15 min before the tests.

2.5. Polarization optical microscopy

Polarization optical images were captured using a polarization optical microscope (POM, model: Nikon E−1000 upright microscope with polarizer). The POM was utilized to examine the microstructures of hardened C–S–H and C–S–H/CNC samples.

2.6. Scanning electron microscopy

Scanning electron microscopy (SEM) was carried out on a Zeiss Auriga FIB/SEM at 5 kV to evaluate the microstructures of the hardened C–S–H and C–S–H/CNC samples. To test the top surface, the hardened samples were horizontally deposited in the holders; to test the cross-section of the C–S–H/CNC-5, the hardened sample was first quenched and broken in liquid nitrogen to obtain the cross-section surface, and then one broken piece was deposited vertically in the holder. All samples were sputtered with Au for 90 s to achieve appropriate conductivity.

2.7. Thermogravimetry analysis

TGA was carried out using a thermal analyzer (model: TA® TG55) to evaluate the organic content and the thermal properties of CNCs, C–S–H, and C–S–H/CNC. For the preparation of samples, 20 mg–50 mg of samples from dried slices were milled into fine powder and vacuum dried for 24 h before the test. During the test, the sample was heated at a constant rate of 20 °C/min from 30 °C to 1,000 °C in a 50 mL/min flow of nitrogen.

2.8. Fourier transform infrared spectroscopy

FTIR was conducted using a Fourier Transform Infrared Spectroscope (model: Bruker Optics Tensor 27 Fourier Transform Infrared Spectrometer) to investigate the chemical structures of CNCs, C–S–H, and C–S–H/CNC, as well as the interaction between C–S–H and CNCs in C–S–H/CNC. The CNCs, C–S–H, and C–S–H/CNC hardened samples were milled into powder samples. Each powder sample was homogeneously mixed with KBr powder and then pressed into pellets for testing. The FTIR spectra were recorded for wavenumbers between 400 cm^{-1} and 4,000 cm^{-1}.

2.9. X-ray diffraction

XRD test was carried out using Cu K radiation source (model: Rigaku Ultima IV X-ray diffractometer, 40 kV, 40 mA) to evaluate the crystalline structures of CNCs, C–S–H, and C–S–H/CNC. The CNCs, C–S–H, and C–S–H/CNC hardened samples were milled into powder. During the XRD tests, each powder sample was scanned on a rotating stage between 2° and 60° (2θ). The step size of scanning was 0.02°, and the time per step was 30 s.

2.10. Atomic force microscopy

Peak-Force quantitative nanomechanics (QNM) was applied to evaluate the elastic modulus of samples using an atomic force micro-

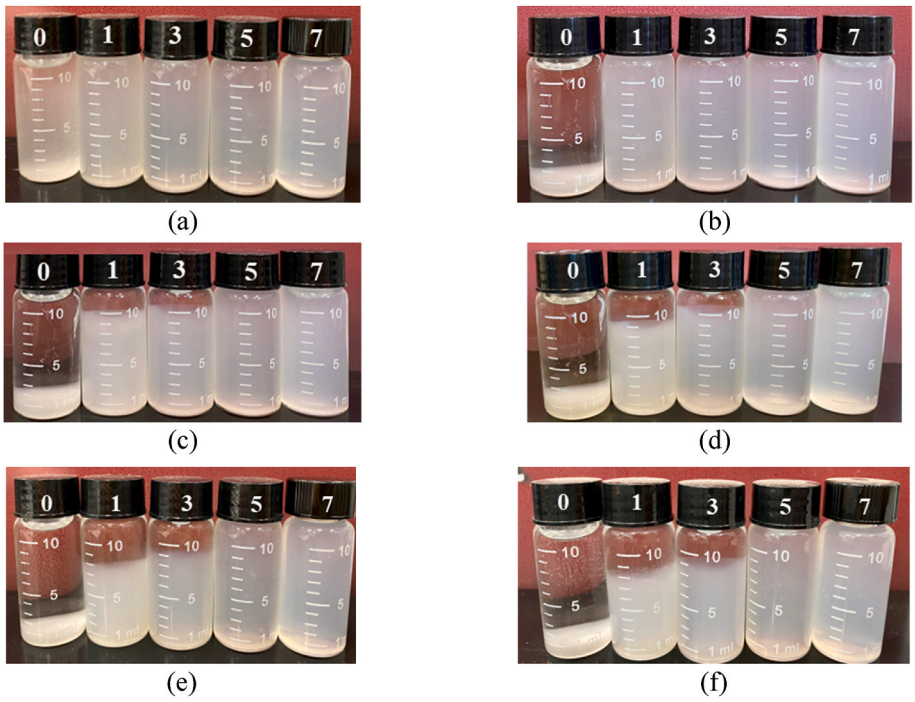

Fig. 4. Visual examination of C–S–H (0), C–S–H/CNC-1 (1), C–S–H/CNC-3 (3), C–S–H/CNC-5 (5), and C–S–H/CNC-7 (7) at (a) 0 h, (b) 6 h, (c) 1 day, (d) 7 days, (e) 3 months, and (f) 6 months.

scope (AFM, model: Bruker Bioscope Resolve AFM with integrated fluorescence microscope). A probe approached the sample surface, indented to a certain depth, and then retracted to the air. In this process, the mechanical response of the local spot was recorded to evaluate the elastic modulus. The elastic modulus was calculated according to Eq. (1) [74].

$$F^{2/3} = \left(\frac{4}{3}\frac{E^*}{(1-\upsilon^2)}\sqrt{R}\right)^{2/3}\delta \tag{1a}$$

$$E^* = \left[\frac{1-\nu_p{}^2}{E_p} + \frac{1-\nu_s{}^2}{E_s}\right]^{-1} \tag{1b}$$

where F is the tip force measured from the AFM probe; E^* is the reduce modulus of tip and sample; υ is the Poisson's ratio of tip and sample; R is the radius of the probe; δ is the indentation depth; ν_p and ν_s are the Poisson's ratios of the probe and the sample, respectively; E_p and E_s are the elastic moduli of the probe and the sample, respectively. The calculation of the elastic modulus was performed using the Nanoscope software.

A diamond probe (DNISP-HS, Bruker) with a stiffness of 360 N/m and a tip radius of 40 nm, as specified by the manufacturer, was used in the nanoindentation tests. The deflection sensitivity was calibrated using a sapphire substrate. The Poisson's ratio of the probe was 0.33. The elastic modulus of the probe is far higher than that of the samples, so Eq. (1b) is rewritten as:

$$E^* = \frac{E_s}{1-\nu_s{}^2} \tag{2}$$

During the test, each sample was scanned by the AFM in an area of 5 μm × 5 μm, with a scanning resolution of 256 × 256, meaning that there were 256 × 256 measurements from each sample. The mean elastic modulus of each sample was obtained using the Nanoscope software [67].

For the preparation of the AFM samples, the C–S–H and C–S–H/CNC hardened samples were deposited in a rubber mold and sealed with epoxy resin. The surface of the samples was polished using abrasive papers (#400, #600, #800, and #1200) on a polish machine (model: Met Prep 3 M polisher). Then, the surface was polished using 1 μm polycrystalline diamond suspension and 0.05 μm FinalPrep Alumina polish solution on a Diamat polishing cloth. Next, each sample was cut into thin disks (thickness: 2–3 mm) and washed with ethanol to remove impurities.

2.11. Three-point bending tests

Three-point bending tests were carried out on a standard mechanical testing machine (Instron 5581 testing system, USA). The hardened C–S–H and C–S–H/CNC-7 were used to fabricate beam specimens for flexural tests. The length, width, and thickness of the beams were 12 mm, 5 mm, and 2 mm, respectively. All tests were performed at a displacement rate of 0.5 mm/min with a support span of 5 mm. The load capacity of the load cell was 500 N. Each test was replicated for five tests. According to ASTM D790-03 [75], the flexural stress (σ) and flexural strain (ε) were respectively calculated using Equation (3) and Equation (4) [75]:

$$\sigma = \frac{3FL}{2bd^2} \tag{3}$$

$$\varepsilon = \frac{6Dd}{L^2} \tag{4}$$

where F is the applied force (N); L is the length of support span, which was 5 mm; b and d are the width and thickness of specimen, which were 5 mm and 2 mm, respectively; and D is the mid-span displacement (mm). The test C–S–H samples were vacuum dried 24 h before three-point bending tests to remove adsorbed water, consistent with the normal operation and testing protocols of cementitious materials samples. The drying operation was conducted at room temperature, rather than elevated temperatures, so the operation did not remove interlayer water and did not affect the microstructure of C–S–H.

Table 1
Stability characteristics of the C–S–H and C–S–H/CNC suspension.

Specimens	Duration of stabilization
C–S–H	<1 h
C–S–H/CNC-1	6–24 h
C–S–H/CNC-3	6–24 h
C–S–H/CNC-5	>6 months
C–S–H/CNC-7	>6 months

3. Experimental results and discussion

3.1. Stability and morphology of C–S–H

When C–S–H was synthesized using $CaCl_2$ and Na_2SiO_3, C–S–H nanoparticles agglomerated into large particles and precipitated immediately after they were produced, as indicated by the loss of transparency of the solutions in Fig. 4(a) and Fig. 4(b). In the presence of CNCs, the transparency of the solutions was largely improved, as shown in Fig. 4(a) and (b), meaning that the use of CNCs hindered the agglomeration of C–S–H nanoparticles. Overall, the stability of the C–S–H suspension increased with the dosage of CNCs, as reflected by the

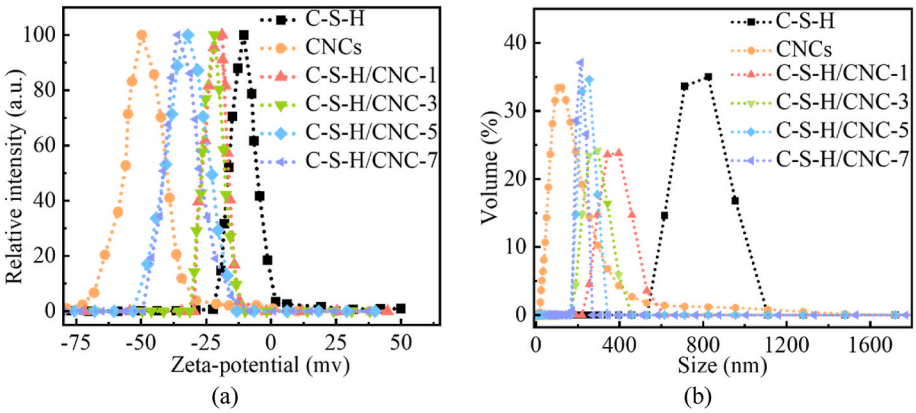

Fig. 5. DLS results: (a) zeta-potential, and (b) dynamic particle size distribution of CNCs, C–S–H, and C–S–H/CNC suspensions.

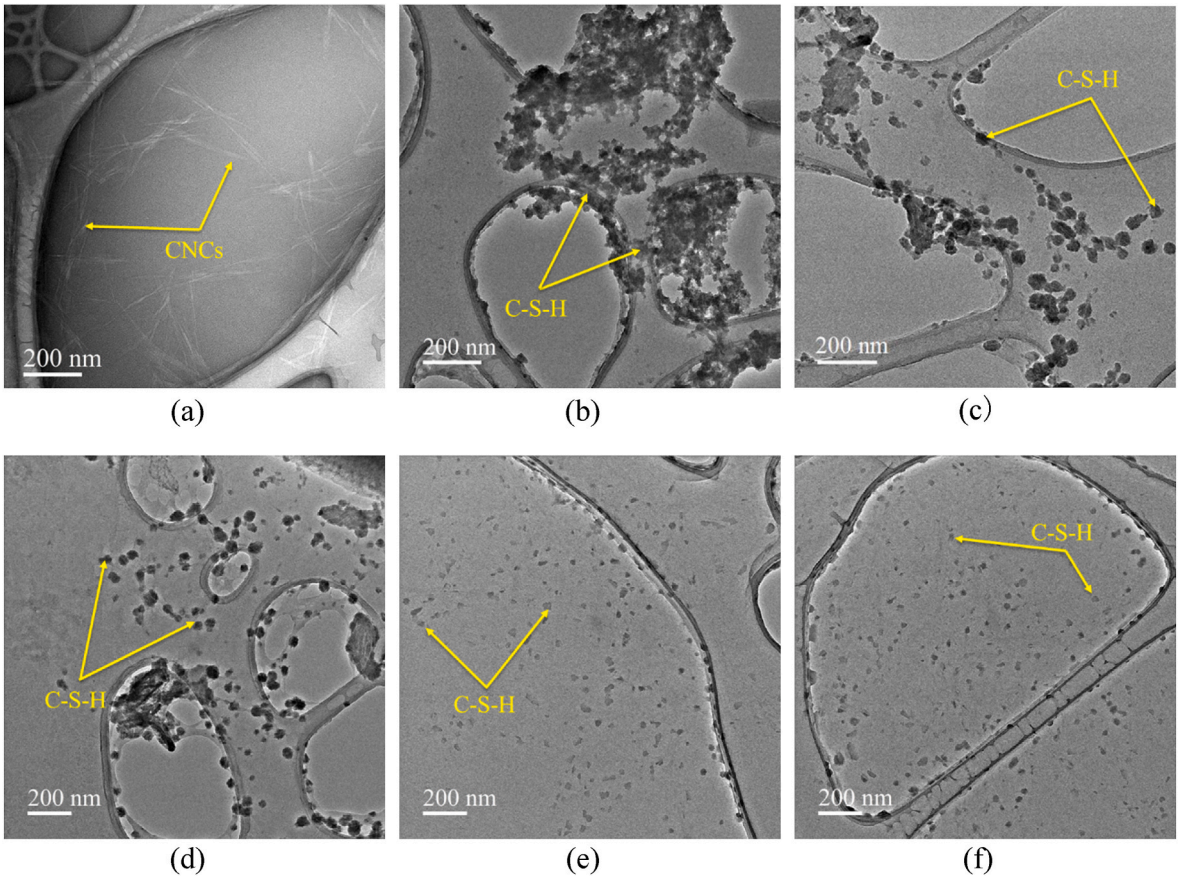

Fig. 6. TEM images of (a) CNCs (20,000X), (b) C–S–H (20,000X), (c) C–S–H/CNC-1 (20,000X), (d) C–S–H/CNC-3 (15,000X), (e) C–S–H/CNC-5 (15,000X), and (f) C–S–H/CNC-7 (15,000X).

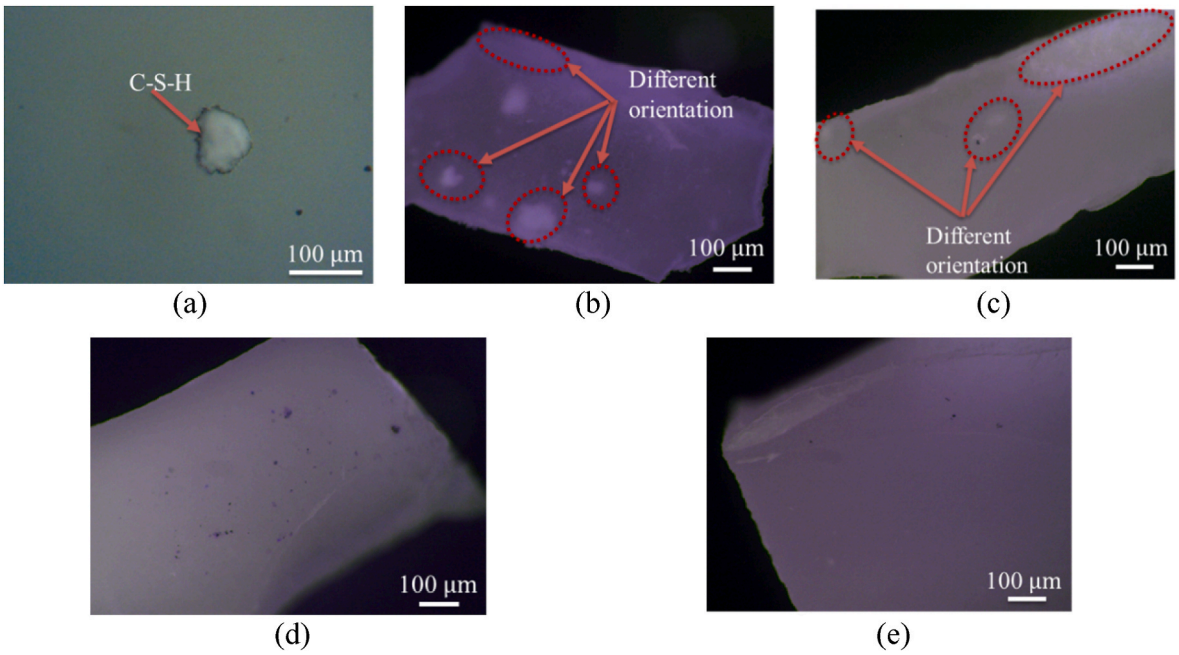

Fig. 7. POM images of (a) C–S–H, (b) C–S–H/CNC-1, (c) C–S–H/CNC-3, (d) C–S–H/CNC-5, and (e) C–S–H/CNC-7.

different levels of transparency in Fig. 4(c)–4(e).

Table 1 compares the stability of different C–S–H suspensions at extended durations based on the photographs in Fig. 4. Without the CNCs, C–S–H lost stability and precipitated immediately. When the dosage of CNCs was up to 3 g/L, the stability of C–S–H/CNC suspensions was retained at 24 h. When the dosage of CNCs was 5 g/L or higher, the stability of C–S–H/CNC suspensions was retained for more than 6 months.

Fig. 5 shows the DLS test results. According to Ref. [76], a suspension is stable when the zeta-potential value exceeds the absolute 25 mV. Without the use of CNCs, the zeta-potential of C–S–H was about −10 mV, due to the partial deprotonation of the silica layers of C–S–H [77], so C–S–H nanoparticles rapidly agglomerated into large C–S–H particles [78]. When CNCs were used, the zeta-potential values of C–S–H/CNC-5 and C–S–H/CNC-7 were lower than −30 mV, so they were stable [79]. The results from the zeta-potential values are consistent with the observation from the photographs shown in Fig. 4.

Due to the secondary nucleation effect of C–S–H and electron attractive forces between nanoparticles, C–S–H nanoparticles tend to agglomerate into large particles and precipitate [78,80]. The dynamic particle sizes of C–S–H aggregates were about 870 nm which means the agglomeration appeared (Fig. 5(b)). As the dosage of CNCs increased from 0 to 7 g/L, the dynamic particle sizes of C–S–H/CNC decreased to about 200 nm, indicating the mitigation of rapid agglomeration. The decrease of the dynamic particle sizes can be attributed to the high negative charges of CNCs that coordinate with the calcium ions of -C-S-H via Ca–O coordination, as well as the interaction between H and O atoms via hydrogen bonds. These mechanisms promote the attachment of CNCs to the surfaces of C–S–H, therefore hindering the secondary nucleation effect and agglomeration of C–S–H [81].

The zeta-potential and dynamic particle size of C–S–H and C–S–H/CNC suspensions were tested again after 6 months synthesis. As shown in Fig. S1(a) and **S1(b)**, there were no significant changes in zeta-potential and dynamic particle size of C–S–H/CNC suspensions, indicating that the addition of CNCs can effectively reduce the agglomeration of C–S–H and keep the suspension stable in a long time.

Fig. 6 shows the morphology of CNCs, C–S–H, and C–S–H/CNC in suspensions under TEM. Fig. 6(a) shows that the CNCs used in this study have a rod-like shape. The lengths are about 100–200 nm, and the diameters are about 5–10 nm. Fig. 6(b) shows C–S–H aggregates without the CNCs. The diameters of the C–S–H aggregates are about 200–800 nm, consistent with reference [9]. Fig. 6(c) and (d) show C–S–H/CNC-1 (1 g/L) and C–S–H/CNC-3 (3 g/L), respectively. The presence of CNCs mitigate the agglomeration of C–S–H nanoparticles. Few C–S–H aggregates are observed, and the sizes of aggregates are largely reduced, compared with the C–S–H aggregates without CNCs. Fig. 6(e) and (f) respectively show C–S–H/CNC-5 (5 g/L) and C–S–H/CNC-7 (7 g/L) that do not show aggregate. The diameters of the C–S–H nanoparticles are about 20–40 nm. The electron intensity transmitted through the C–S–H nanoparticles is uniform, revealing that their thicknesses are relatively uniform, different from the nonuniform electron intensity of C–S–H aggregates in Fig. 6(b). The TEM results corroborate that CNCs hinder the agglomeration of C–S–H nanoparticles.

Fig. 6(c) to **6(f)** do not show CNCs clearly due to the different contrasts of CNCs and C–S–H. To reveal the relative positions of CNCs and C–S–H, a lower magnification factor was used for the TEM images, as shown in Fig. S2. It was found that some CNCs passed through C–S–H, and some CNCs were adsorbed on the surfaces of C–S–H, indicating that CNCs interact with C–S–H through interfacial Ca–O coordination and hydrogen bonds. This mechanism hinders the agglomeration of C–S–H. The rod-like CNCs also provide steric repulsion to reduce the attractive forces of C–S–H nanoparticles, further suppressing the agglomeration.

To evaluate the long-term stability of C–S–H/CNC suspensions, the C–S–H/CNC-5 suspension was examined after 3 months. Fig. S3 shows the TEM image of dispersed C–S–H nanoparticles with diameters of 20–40 nm, the same as their diameters observed 3 months ago (Fig. 6 (e)), revealing desired long-term stability of the C–S–H/CNC suspension.

3.2. Microstructures of C–S–H and C–S–H/CNCs

Fig. 7 shows the POM results. No polarization is observed from the C–S–H specimen without CNCs (Fig. 7(a)), indicating that the C–S–H aggregates had random orientations due to the spatially-disordered microstructures formed during the rapid agglomeration.

The C–S–H/CNC specimens show regulated orientations, indicating ordered microstructures (Fig. 7(b)–7(e)). The images of C–S–H/CNC-1 and C–S–H/CNC-3 show bright spots locally (Fig. 7(b) and (c)), indicating variations of orientation on a microscale. The images of C–S–H/

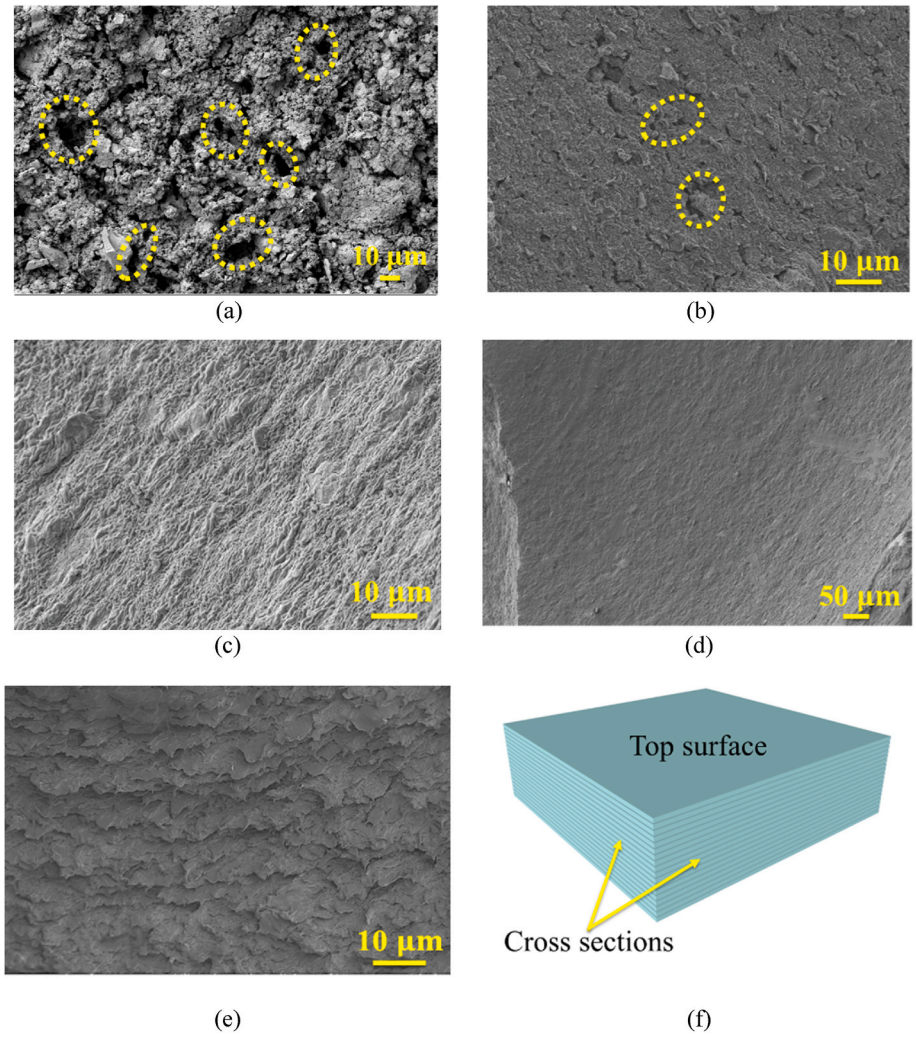

Fig. 8. SEM images: (a) top surface of C–S–H (500X), (b) top surface of C–S–H/CNC-1 (1,000X), (c) top surface of C–S–H/CNC-5 (1,000X), (d) top surface of C–S–H/CNC-5 (100X), (e) cross section of C–S–H/CNC-5 (1,000X), and (f) illustration of the top surface and cross sections of the specimens. The dotted circles in (a) and (b) point out the agglomeration in the hardened samples.

CNC-5 and C–S–H/CNC-7 show uniform colors on a millimeter scale (Fig. 7(d) and (e)), confirming long-range oriented microstructures.

The microstructures were further assessed via SEM, as shown in Fig. 8. The C–S–H specimen exhibits many pores with a random spatial distribution, revealing that the microstructures of C–S–H aggregates are disordered and porous (Fig. 8(a)). The C–S–H/CNC specimens show refined microstructures with lower porosity and smaller pore sizes (Fig. 8(b) to 8(e)). Minor localized aggregations and pores are observed from the C–S–H/CNC-1 specimen (Fig. 8(b)), and the pore sizes are significantly smaller than those of the C–S–H specimen.

No aggregation was found from the C–S–H/CNC-5 specimen (Fig. 8 (c)–8(e)), and the specimen exhibits dense microstructures. Most notably, the C–S–H/CNC-5 specimen shows no pores on the micrometer scale (Fig. 8(d)) indicating its capability to reduce the crack form and propagation. The cross section of the C–S–H/CNC-5 specimen exhibits densely-packed layered microstructures (Fig. 8(e)). The top surface and cross sections of the C–S–H/CNC specimens are illustrated in Fig. 8(f). Such dense, layered microstructure is similar to a "nacre-like" structure which can effectively minimize the usual pores and defects in C–S–H and lead to an improvement in mechanical properties [82].

Fig. 9 illustrates the microstructures of C–S–H, according to the results from TEM, POM, and SEM characterization. When CNCs are not used, the C–S–H nanoparticles rapidly agglomerate and precipitate as C–S–H aggregates with random, porous microstructures. The C–S–H aggregates loosely stack in the filtration process, forming porous microstructures (Fig. 9(a)). In the presence of CNCs, rapid agglomeration of C–S–H is suppressed by strong interfacial interactions between C–S–H and CNCs (Fig. 9(b)). The C–S–H nanoparticles stack in the filtration process, forming layered dense microstructures. The rigid CNCs provide interlayer bridging between C–S–H layers and promote their spatial alignment, generating dense layered microstructures. Further discussions on the chemical bonds are provided in section 3.3.

3.3. Chemical structure, crystallization, and composition

The effects of CNCs on the chemical structure, crystallization, and composition of C–S–H were further investigated through FTIR, XRD, and TGA, respectively. Fig. 10(a) shows the FTIR results of C–S–H, CNCs, and C–S–H/CNC specimens. Table 2 lists the five main peaks of C–S–H, consistent with reference [83]. CNCs show seven main peaks. C–S–H/CNCs shows ten main peaks, covering all the peaks of C–S–H and CNCs.

Compared with the peaks of C–S–H, the C–S–H/CNC specimens with increased CNC content show a shift of the O–H peak to lower wavenumbers (from 3,470 cm^{-1} to 3,430 cm^{-1}). Such a shift is attributed to the formation of hydrogen bonds and calcium ion coordination bonds between CNCs and C–S–H, as shown in Fig. 9(b) [84–86]. Calcium ion coordination bonds refer to the ion coordination bonds between the –OH

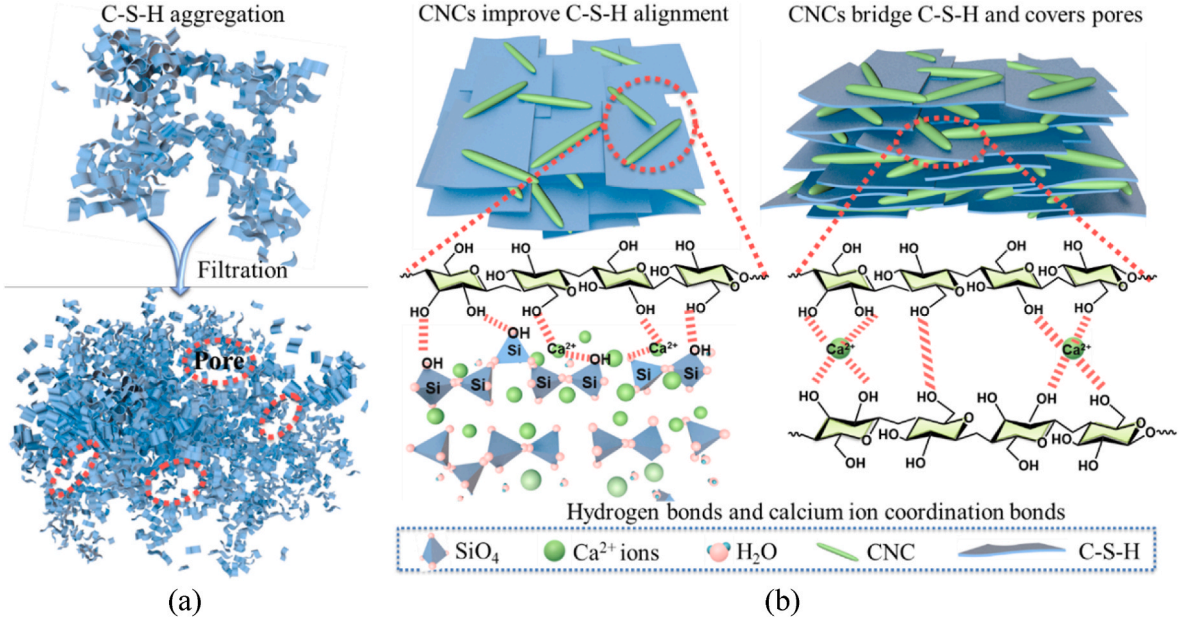

Fig. 9. Illustration of the formation process of (a) C–S–H, and (b) C–S–H/CNC.

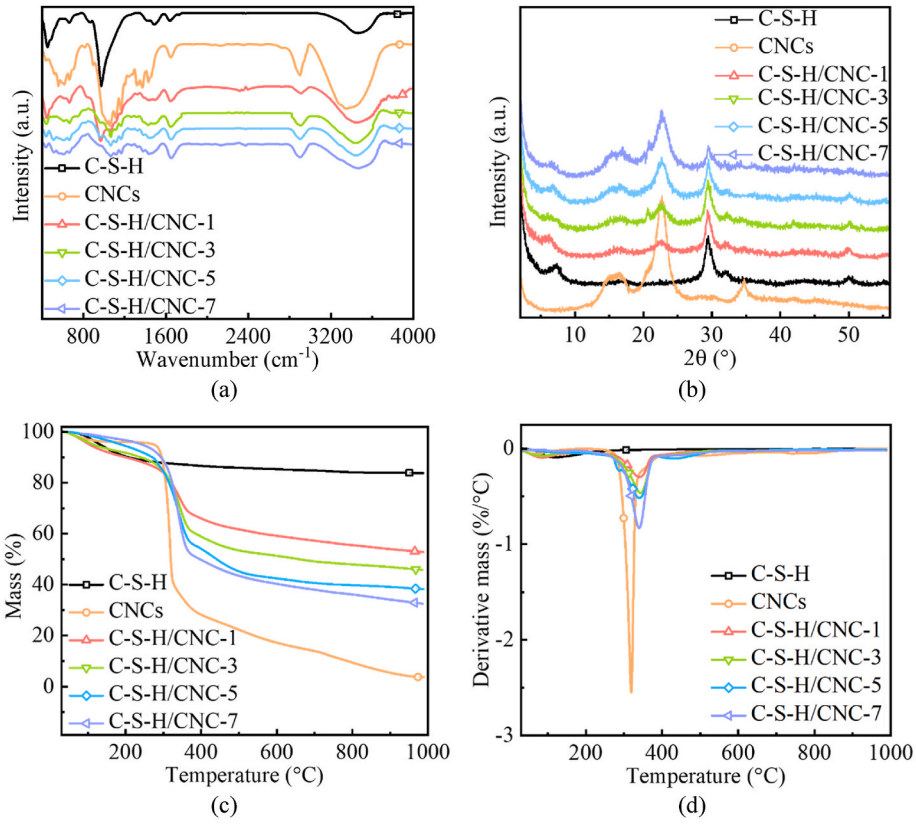

Fig. 10. Characterization of the chemical structure, crystallization, and composition of C–S–H and C–S–H/CNC: (a) FTIR results, (b) XRD results, (c) TGA results, and (d) derivative of TGA.

groups on the surface of CNCs and the calcium ions of C–S–H [84–86]. As the content of CNCs increased from 0 to 7 g/L, the magnitudes of peaks of C–S–H decreased due to the decrease of the C–S–H proportion in C–S–H/CNC nanocomposites.

The crystallization structures of C–S–H, CNCs, and C–S–H/CNC were characterized through XRD, as shown in Fig. 10(b). The XRD spectra of the C–S–H/CNC samples are similar to the XRD spectra of C–S–H and CNCs. There is no new diffraction peak, indicating that the addition of CNCs does not change the crystalline structure of C–S–H. The crystalline structures of C–S–H/CNC are similar to the crystalline structure of C–S–H. The C–S–H exhibits a defective tobermorite structure [87–89]. The diffraction peaks at 6 ° to 9 ° reflect the interlayer spacing of C–S–H crystals [64,70]. The XRD results show that the interlayer spacing of C–S–H/CNC is comparable with that of C–S–H, revealing that CNCs are

Table 2
Peaks in the FTIR curves.

	Wavenumber (cm^{-1})	Duration of stabilization
C–S–H	457	O–Si–O deformation of SiO_4 tetrahedra
	800	Si–O stretching vibrations of the Q^1 tetrahedra
	970	Si–O asymmetric stretching vibrations of Q^2 tetrahedra
	1,640	H–O–H bending vibrations in water
	3,470	O–H stretching vibrations in water or C–S–H
CNCs	1,080	C–C stretching vibrations of CNCs
	1,175	C–O stretching vibrations of CNCs
	1,375/1,460/ 2,900	C–H symmetric stretching, in-plane bending, and deformation vibrations of CNCs
	1,640	H–O–H bending vibrations in water
	3,340	O–H stretching vibrations in water or CNCs
C–S–H/ CNC	457	O–Si–O deformation of SiO_4 tetrahedra
	800	Si–O stretching vibrations of the Q^1 tetrahedra
	970	Si–O asymmetric stretching vibrations of Q^2 tetrahedra
	1,080	C–C stretching vibrations of CNCs
	1,175	C–O stretching vibrations of CNCs
	1,375/1,460/ 2,900	C–H symmetric stretching, in-plane bending, and deformation vibrations of CNCs
	1,640	H–O–H bending vibrations in water
	3,430	O–H stretching vibrations of water, C–S–H, or CNCs

adsorbed to the surfaces of C–S–H, rather than intercalating into the interlayer structure of C–S–H, because intercalation will change the interlayer spacing. Such results can be attributed to the morphology of CNCs. The diameters of rod-like CNCs are 5–10 nm, larger than the interlayer spacing of C–S–H (about 1.1 nm–1.4 nm) [64,70]. The absorption mechanism is that the hydroxyl groups of CNCs can complex Ca^{2+} via calcium ion coordination bonds and interact with $H_3SO_4^-$ via hydrogen bonds which can make CNCs absorbed on the surface of C–S–H [70]. As discussed above, the absorption of CNCs can provide steric effect to suppress the agglomeration of CNCs, and CNCs can also act as a bridge to promote the spatial alignment of C–S–H.

The chemical composition of C–S–H and C–S–H/CNC were evaluated via TGA. The results are shown in Fig. 10(c). The mass loss of CNCs is analyzed at three levels of temperature: (1) 30–200 °C: the evaporation of water; (2) 200–600 °C: the dehydration and decomposition of CNCs [90,91]; and (3) 600–1000 °C: the aromatization of CNCs [60]. The mass loss of C–S–H mainly occurred at 30–200 °C due to the loss of water, and a mass loss of 20% was measured. The mass loss of C–S–H/CNC is analyzed at three levels of temperature: (1) 30–300 °C: the evaporation of water and dehydration of C–S–H and CNCs [92]; (2) 200–600 °C: the decomposition of CNCs and dehydration of C–S–H; (3) 600–1000 °C: the aromatization of CNCs. As the content of CNCs increased from 1 g/L to 7 g/L, the mass loss increased, because of the increased dosage of CNCs. The major mass loss of C–S–H/CNC occurs at around 340 °C, higher than that of CNCs (310 °C), meaning that the interactions between C–S–H and CNCs via hydrogen bond and calcium ion coordination bond improved the thermal stability of the C–S–H/CNC (Fig. 10(d)). The derivative TGA curves show two major endothermic peaks at 30–300 °C and 200–600 °C. The two peaks can be attributed to the dehydration and decomposition of C–S–H and CNCs at elevated temperatures [93].

3.4. Mechanical properties

The elastic moduli of C–S–H and C–S–H/CNC were evaluated through AFM nanoindentation. Fig. 11 shows the Gauss fitting-based statistics of elastic moduli. More details about Gauss fitting are presented in Table S1. The mean value of the elastic modulus of C–S–H is 19 GPa, consistent with the values (16–35 GPa) in Refs. [94–96]. The mean values of the elastic moduli of C–S–H/CNC increase with the content of CNCs from 0 to 7 g/L. The mean value of the elastic modulus of C–S–H/CNC-7 is 56 GPa, which is 2.9 times that of C–S–H.

The improvement of the elastic modulus is attributed to the reinforcing effect of CNCs whose elastic modulus is around 140 GPa [97,98]. Besides, the pores also have an important effect on the elastic modulus.

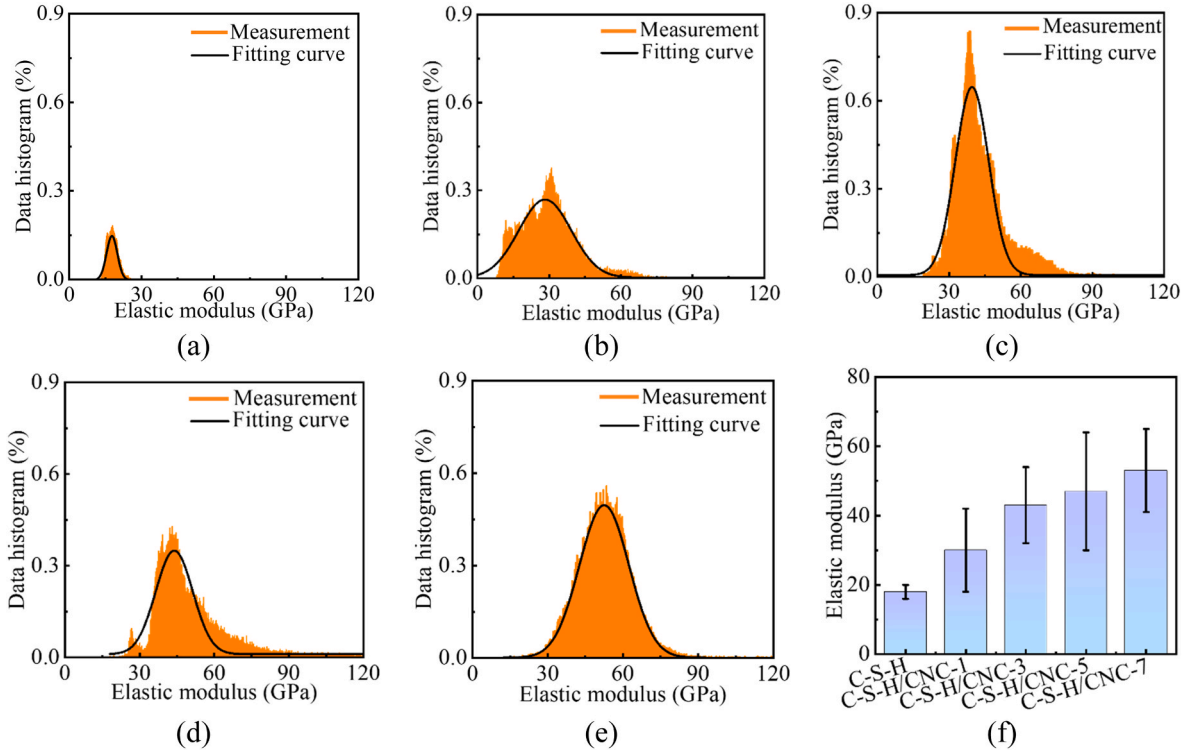

Fig. 11. AFM results of the elastic moduli of: (a) C–S–H, (b) C–S–H/CNC-1, (c) C–S–H/CNC-3, (d) C–S–H/CNC-5, and (e) C–S–H/CNC-7; and (f) mean values of the elastic moduli of C–S–H and C–S–H/CNCs. Error bars represent the standard deviations.

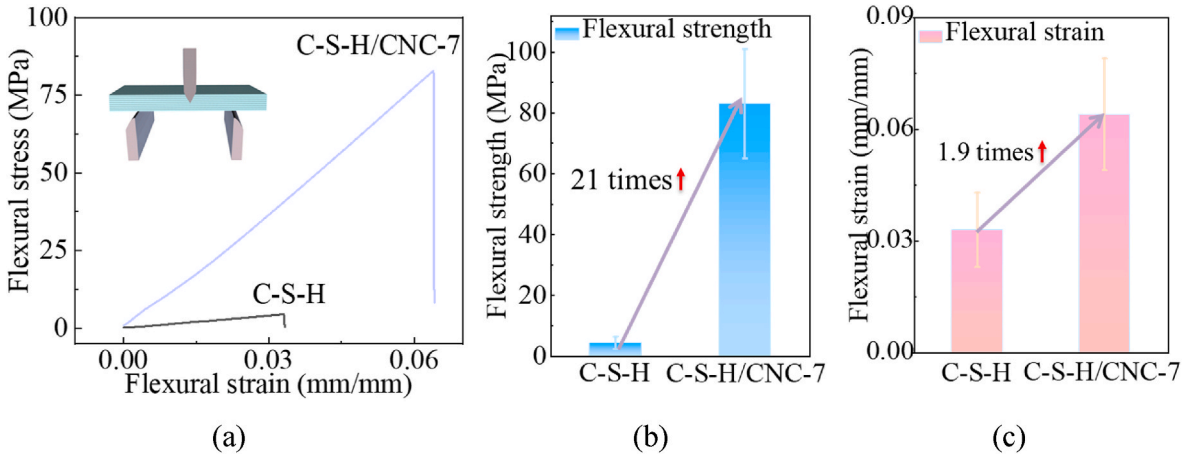

Fig. 12. Flexural test results of C–S–H and C–S–H/CNC-7: (a) flexural stress and strain curves; (b) flexural strengths; and (c) flexural strains.

The consequence of SEM showed that the CNCs effectively diminished the pores which also increased the elastic modulus. Furthermore, the strong interfacial interactions between C–S–H and CNCs can further improve the elastic modulus of C–S–H/CNC.

The flexural strength and flexural strain of C–S–H and C–S–H/CNC-7 were evaluated through three-point bending tests. Fig. 12(a) shows the stress-strain curves. It was worth noting that such C–S–H/CNC nanocomposite simultaneously achieved high flexural strength and flexural strain. The flexural strength of the pure C–S–H was 4 MPa, which is consistent with the value of reference (2–6 MPa) [99]. The flexural strain of the pure C–S–H was 0.033 mm/mm. For C–S–H/CNC-7, the flexural strength and flexural strain were 83 MPa and 0.064 mm/mm, respectively. Compared with the pure C–S–H, the values of flexural strength and flexural strain of C–S–H/CNC-7 were 21 and 1.9 times as high as those of pure C–S–H, respectively, as shown in Fig. 12(b) and (c). Such results can be attributed to the dense and layered microstructures of C–S–H/CNC. Besides, the rod-like CNCs with large aspect ratio (10–40) and high tensile strength (7–10 GPa) can bridge nano/-microcracks, thus slowing the crack formation and propagation [26, 100].

4. Conclusions

Based on the above investigations, the following conclusions are drawn:

- CNCs can suppress the agglomeration of C–S–H nanoparticles. As the dosage of CNCs was increased from 0 to 5 g/L, the stability of C–S–H nanoparticles was largely improved. When the dosage of CNCs reached 5 g/L, the C–S–H suspension was stable for more than 6 months. Increasing the dosage of CNCs from 5 g/L to 7 g/L sustained the stability of the C–S–H suspension. The diameters of stabilized C–S–H nanoparticles were about 20–40 nm, much finer than the diameters (larger than 800 nm) of agglomerated C–S–H aggregates. The stabilized C–S–H nanoparticles suspended and formed C–S–H/CNC suspensions.
- Hardened C–S–H/CNC can be produced via the filtration of C–S–H/CNC suspensions. The generated C–S–H/CNC specimens showed spatially-ordered layered dense microstructures. Compared with C–S–H specimens with random porous microstructures, the C–S–H/CNC nanocomsposites were dense and oriented.
- CNCs interact with C–S–H via hydrogen bonds and ion coordination bonds. In the C–S–H/CNC specimens, CNCs were adsorbed to the surfaces of C–S–H rather than intercalating inside of C–S–H. This was revealed by the comparable interlayer spacing of C–S–H and C–S–H/CNC.
- The C–S–H/CNC nanocomposites achieved higher strength and flexibility, simultaneously, than those of C–S–H. As the dosage of CNCs increased from 1 g/L to 7 g/L, the elastic modulus was increased from 30 GPa to 56 GPa, which is 2.9 times that of C–S–H. Besides, the flexural strength and flexural strain of C-SH/CNC-7 were 21 and 1.9 times higher than those of pure C–S–H. The enhancement is attributed to the ordered, layered, and dense microstructures of C–S–H/CNC and the high elastic modulus of CNCs.

Future work

Further research will be conducted to investigate how the highly ordered, layered, and dense microstructure, such as the layer thickness, the orientation of the microstructure, and the large-scale factors affect the mechanical properties (i.e., elastic modulus, flexural properties) of C–S–H.

Declaration of competing interest

The authors declare that they have no known competing financial interests or personal relationships that could have appeared to influence the work reported in this paper.

Data availability

Data will be made available on request.

Acknowledgement

This research was funded by the National Science Foundation [award No. = CMMI 2046407], United States. The authors thank Dr. Tsengming Chou, from the Laboratory for Multi-scale Imaging, who helped the SEM and TEM testing. The authors would like to thank Dr. Jongyoun Son and Dr. Jiaqi Lv, from the Microdevice Laboratory, who helped polish the AFM samples. The authors also would like to thank Dr. Jiang Du and Dr. Xiao Tan, who helped with the three-point bending tests.

Appendix A. Supplementary data

Supplementary data to this article can be found online at https://doi.org/10.1016/j.cemconcomp.2023.105276.

References

[1] Y. Zhang, S. Zhang, X. Jiang, Q. Chen, Z. Jiang, J.W. Ju, M. Bauchy, Insights into the thermal effect on the fracture toughness of calcium silicate hydrate grains: a reactive molecular dynamics study, Cement Concr. Compos. 134 (2022), 104824.

[2] J. Starr, E. Soliman, E. Matteo, T. Dewers, J. Stormont, M.R. Taha, Mechanical characterization of low modulus polymer-modified calcium-silicate-hydrate (C–S–H) binder, Cement Concr. Compos. 124 (2021), 104219.
[3] I. Richardson, Tobermorite/jennite-and tobermorite/calcium hydroxide-based models for the structure of CSH: applicability to hardened pastes of tricalcium silicate, β-dicalcium silicate, Portland cement, and blends of Portland cement with blast-furnace slag, metakaolin, or silica fume, Cement Concr. Res. 34 (9) (2004) 1733–1777.
[4] Z. Zhang, G.W. Scherer, A. Bauer, Morphology of cementitious material during early hydration, Cement Concr. Res. 107 (2018) 85–100.
[5] J. Rieger, M. Kellermeier, L. Nicoleau, Formation of nanoparticles and nanostructures—an industrial perspective on $CaCO_3$, cement, and polymers, Angew. Chem. Int. Ed. 53 (46) (2014) 12380–12396.
[6] A. Morshedifard, S. Masoumi, M.A. Qomi, Nanoscale origins of creep in calcium silicate hydrates, Nat. Commun. 9 (1) (2018) 1–10.
[7] K. Ioannidou, M. Kanduč, L. Li, D. Frenkel, J. Dobnikar, E. Del Gado, The crucial effect of early-stage gelation on the mechanical properties of cement hydrates, Nat. Commun. 7 (1) (2016) 1–9.
[8] M. Theobald, J. Plank, C–S–H–Polycondensate nanocomposites as effective seeding materials for Portland composite cements, Cement Concr. Compos. 125 (2022), 104278.
[9] V. Kanchanason, J. Plank, Role of pH on the structure, composition and morphology of CSH–PCE nanocomposites and their effect on early strength development of Portland cement, Cement Concr. Res. 102 (2017) 90–98.
[10] J. Sun, H. Shi, B. Qian, Z. Xu, W. Li, X. Shen, Effects of synthetic CSH/PCE nanocomposites on early cement hydration, Construct. Build. Mater. 140 (2017) 282–292.
[11] J. Sun, H. Dong, J. Wu, J. Jiang, W. Li, X. Shen, G. Hou, Properties evolution of cement-metakaolin system with CSH/PCE nanocomposites, Construct. Build. Mater. 282 (2021), 122707.
[12] V. Kanchanason, J. Plank, Effect of calcium silicate hydrate–polycarboxylate ether (CSH–PCE) nanocomposite as accelerating admixture on early strength enhancement of slag and calcined clay blended cements, Cement Concr. Res. 119 (2019) 44–50.
[13] M. Schönlein, J. Plank, A TEM study on the very early crystallization of CSH in the presence of polycarboxylate superplasticizers: transformation from initial CSH globules to nanofoils, Cement Concr. Res. 106 (2018) 33–39.
[14] Z. You, J. Xu, Investigation on variables contributing to the synthesis of CSH/PCE nanocomposites by co-precipitation method, Materials 14 (24) (2021) 7673.
[15] F. Zou, M. Zhang, C. Hu, F. Wang, S. Hu, Novel CASH/PCE nanocomposites: design, characterization and the effect on cement hydration, Chem. Eng. J. 412 (2021), 128569.
[16] Y. Zhou, C.A. Orozco, E. Duque-Redondo, H. Manzano, G. Geng, P. Feng, P. J. Monteiro, C. Miao, Modification of poly (ethylene glycol) on the microstructure and mechanical properties of calcium silicate hydrates, Cement Concr. Res. 115 (2019) 20–30.
[17] Y. Zhou, D. Hou, J. Jiang, W. She, J. Yu, Reactive molecular simulation on the calcium silicate hydrates/polyethylene glycol composites, Chem. Phys. Lett. 687 (2017) 184–187.
[18] H. Matsuyama, J.F. Young, Synthesis of calcium silicate hydrate/polymer complexes: Part I. Anionic and nonionic polymers, J. Mater. Res. 14 (8) (1999) 3379–3388.
[19] Z. Zhu, Z. Wang, Y. Zhou, Y. Wei, A. She, Synthesis and structure of calcium silicate hydrate (CSH) modified by hydroxyl-terminated polydimethylsiloxane (PDMS), Construct. Build. Mater. 267 (2021), 120731.
[20] Z. Zhu, Y. Zhou, Z. Huang, Z. Wang, Y. Chen, Mechanical properties evaluation of polymer-binding CSH structure from nanoscale to macroscale: hydroxyl-terminated polydimethylsiloxane (PDMS) modified CSH, Materials 15 (23) (2022) 8361.
[21] Y. Zhou, L. Tang, J. Liu, C. Miao, Interaction mechanisms between organic and inorganic phases in calcium silicate hydrates/poly (vinyl alcohol) composites, Cement Concr. Res. 125 (2019), 105891.
[22] S. Mojumdar, L. Raki, Preparation and properties of calcium silicate hydrate-poly (vinyl alcohol) nanocomposite materials, J. Therm. Anal. Calorim. 82 (1) (2005) 89–95.
[23] S. Ding, D. Fang, Z. Pang, B. Luo, L. Kuang, H. Wang, Q. Zhang, Q. Shen, F. Ji, Immobilization of powdery calcium silicate hydrate via PVA covalent cross-linking process for phosphorus removal, Sci. Total Environ. 645 (2018) 937–945.
[24] Y. Zhang, X. Kong, Correlations of the dispersing capability of NSF and PCE types of superplasticizer and their impacts on cement hydration with the adsorption in fresh cement pastes, Cement Concr. Res. 69 (2015) 1–9.
[25] E. Cappelletto, S. Borsacchi, M. Geppi, F. Ridi, E. Fratini, P. Baglioni, Comb-shaped polymers as nanostructure modifiers of calcium silicate hydrate: a ^{29}Si solid-state NMR investigation, J. Phys. Chem. C 117 (44) (2013) 22947–22953.
[26] W. Meng, K.H. Khayat, Mechanical properties of ultra-high-performance concrete enhanced with graphite nanoplatelets and carbon nanofibers, Compos. B Eng. 107 (2016) 113–122.
[27] J. Du, W. Meng, K.H. Khayat, Y. Bao, P. Guo, Z. Lyu, A. Abu-obeidah, H. Nassif, H. Wang, New development of ultra-high-performance concrete (UHPC), Compos. B Eng. 224 (2021), 109220.
[28] Z. Liu, H. Ge, J. Wu, J. Chen, Enhanced electromagnetic interference shielding of carbon fiber/cement composites by adding ferroferric oxide nanoparticles, Construct. Build. Mater. 151 (2017) 575–581.
[29] A. Dinesh, B. Abirami, G. Moulica, Carbon nanofiber embedded cement composites: properties and promises as sensor–a review, Mater. Today: Proc. 44 (2021) 4166–4172.
[30] X. Zhu, Y. Gao, Z. Dai, D.J. Corr, S.P. Shah, Effect of interfacial transition zone on the Young's modulus of carbon nanofiber reinforced cement concrete, Cement Concr. Res. 107 (2018) 49–63.
[31] Y. Gao, H. Jing, Z. Yu, L. Li, J. Wu, W. Chen, Particle size distribution of aggregate effects on the reinforcing roles of carbon nanotubes in enhancing concrete ITZ, Construct. Build. Mater. 327 (2022), 126964.
[32] A. Carriço, J. Bogas, A. Hawreen, M. Guedes, Durability of multi-walled carbon nanotube reinforced concrete, Construct. Build. Mater. 164 (2018) 121–133.
[33] M. Krystek, D. Pakulski, V. Patroniak, M. Górski, L. Szojda, A. Ciesielski, P. Samorì, High-performance graphene-based cementitious composites, Adv. Sci. 6 (9) (2019), 1801195.
[34] K. Barri, Q. Zhang, J. Kline, W. Lu, J. Luo, Z. Sun, B.E. Taylor, S.G. Sachs, L. Khazanovich, Z.L. Wang, Multifunctional nanogenerator-integrated metamaterial concrete systems for smart civil infrastructure, Adv. Mater. (2023), 2211027.
[35] Z. Pan, L. He, L. Qiu, A.H. Korayem, G. Li, J.W. Zhu, F. Collins, D. Li, W.H. Duan, M.C. Wang, Mechanical properties and microstructure of a graphene oxide–cement composite, Cement Concr. Compos. 58 (2015) 140–147.
[36] S. Chuah, Z. Pan, J.G. Sanjayan, C.M. Wang, W.H. Duan, Nano reinforced cement and concrete composites and new perspective from graphene oxide, Construct. Build. Mater. 73 (2014) 113–124.
[37] Y. Suo, R. Guo, H. Xia, Y. Yang, B. Zhou, Z. Zhao, A review of graphene oxide/cement composites: performance, functionality, mechanisms, and prospects, J. Build. Eng. 53 (2022), 104502.
[38] P. Abhilash, D.K. Nayak, B. Sangoju, R. Kumar, V. Kumar, Effect of nano-silica in concrete; a review, Construct. Build. Mater. 278 (2021), 122347.
[39] K. Khan, W. Ahmad, M.N. Amin, S. Nazar, Nano-silica-modified concrete: a bibliographic analysis and comprehensive review of material properties, Nanomaterials 12 (12) (2022) 1989.
[40] D. Kong, S. Huang, D. Corr, Y. Yang, S.P. Shah, Whether do nano-particles act as nucleation sites for CSH gel growth during cement hydration? Cement Concr. Compos. 87 (2018) 98–109.
[41] A. Hanif, Z. Lu, P. Parthasarathy, D. Hou, Z. Li, G. Sun, Strength and hydration attributes of cement pastes containing nano titania and cenosphere, Adv. Cement Res. 32 (12) (2020) 557–572.
[42] Q. Fu, Z. Zhang, X. Zhao, W. Xu, D. Niu, Effect of nano calcium carbonate on hydration characteristics and microstructure of cement-based materials: a review, J. Build. Eng. 50 (2022), 104220.
[43] Z. Liu, J. Du, W. Meng, Achieving low-carbon cementitious materials with high mechanical properties using $CaCO_3$ suspension produced by CO_2 sequestration, J. Clean. Prod. 373 (2022), 133546.
[44] F. Basquiroto de Souza, E. Shamsaei, S. Chen, K. Sagoe-Crentsil, W. Duan, Controlled growth and ordering of poorly-crystalline calcium-silicate-hydrate nanosheets, Commun. Mater. 2 (1) (2021) 1–11.
[45] X. Kang, X. Zhu, J. Qian, J. Liu, Y. Huang, Effect of graphene oxide (GO) on hydration of tricalcium silicate (C_3S), Construct. Build. Mater. 203 (2019) 514–524.
[46] Y. Li, H. Li, C. Jin, Z. Wang, J. Hao, Y. Li, J. Liu, Multi-scale investigation and mechanism analysis on Young's modulus of CSH modified by multi-walled carbon nanotubes, Construct. Build. Mater. 308 (2021), 125079.
[47] J. Wang, B. Han, Z. Li, X. Yu, X. Dong, Effect investigation of nanofillers on CSH gel structure with Si NMR, J. Mater. Civ. Eng. 31 (1) (2019), 04018352.
[48] X. Wang, D. Feng, X. Shi, J. Zhong, Carbon nanotubes do not provide strong seeding effect for the nucleation of C_3S hydration, Mater. Struct. 55 (7) (2022) 1–17.
[49] J. Li, Q. Zheng, The first experimental evidence for improved nanomechanical properties of calcium silicate hydrate by polycarboxylate ether and graphene oxide, Cement Concr. Res. 156 (2022), 106787.
[50] L. Nicoleau, T. Gädt, L. Chitu, G. Maier, O. Paris, Oriented aggregation of calcium silicate hydrate platelets by the use of comb-like copolymers, Soft Matter 9 (19) (2013) 4864–4874.
[51] J. Wu, Y.-J. Zhu, F. Chen, X.-Y. Zhao, J. Zhao, C. Qi, Amorphous calcium silicate hydrate/block copolymer hybrid nanoparticles: synthesis and application as drug carriers, Dalton Trans. 42 (19) (2013) 7032–7040.
[52] Y. Li, H. Li, Z. Wang, C. Jin, Effect and mechanism analysis of functionalized multi-walled carbon nanotubes (MWCNTs) on CSH gel, Cement Concr. Res. 128 (2020), 105955.
[53] D. Hou, G. Qiao, P. Wang, Load transfer mechanism at the calcium silicate hydrate/carbon nanotubes interface changed by carbon nanotubes surface modification investigated from atomic simulation, Appl. Surf. Sci. 594 (2022), 153487.
[54] A. Gholampour, M. Valizadeh Kiamahalleh, D.N. Tran, T. Ozbakkaloglu, D. Losic, From graphene oxide to reduced graphene oxide: impact on the physiochemical and mechanical properties of graphene–cement composites, ACS Appl. Mater. Interfaces 9 (49) (2017) 43275–43286.
[55] S. Li, H. Li, X. Wang, Y. Song, Y. Liu, L. Jiang, D. Zhu, Super-hydrophobicity of large-area honeycomb-like aligned carbon nanotubes, J. Phys. Chem. B 106 (36) (2002) 9274–9276.
[56] G. Hummer, J.C. Rasaiah, J.P. Noworyta, Water conduction through the hydrophobic channel of a carbon nanotube, Nature 414 (6860) (2001) 188–190.
[57] M. Sharma, S. Gao, E. Mäder, H. Sharma, L.Y. Wei, J. Bijwe, Carbon fiber surfaces and composite interphases, Compos. Sci. Technol. 102 (2014) 35–50.
[58] Y. Habibi, L.A. Lucia, O.J. Rojas, Cellulose nanocrystals: chemistry, self-assembly, and applications, Chem. Rev. 110 (6) (2010) 3479–3500.
[59] Y. Wang, R. Xie, S. Zheng, N. Zhou, J. Lu, I. Ahmad, L. Gan, J. Huang, Nonuniformly modifying high-aspect-ratio rigid cellulose nanocrystals to enhance

percolation advantage in weakly compatible biomass polymer systems, Cellulose 28 (8) (2021) 4655–4669.
[60] D. Trache, A.F. Tarchoun, M. Derradji, O. Mehelli, M.H. Hussin, W. Bessa, Cellulose Fibers and Nanocrystals: Preparation, Characterization, and Surface Modification, Functionalized Nanomaterials I, CRC Press, 2020, pp. 171–190.
[61] Y. Cao, P. Zavaterri, J. Youngblood, R. Moon, J. Weiss, The influence of cellulose nanocrystal additions on the performance of cement paste, Cement Concr. Compos. 56 (2015) 73–83.
[62] S. Atifi, M.N. Mirvakili, C.A. Williams, M.M. Bay, S. Vignolini, W.Y. Hamad, Fast Self-Assembly of scalable photonic cellulose nanocrystals and hybrid films via electrophoresis, Adv. Mater. 34 (12) (2022), 2109170.
[63] E. Cuenca, A. Mezzena, L. Ferrara, Synergy between crystalline admixtures and nano-constituents in enhancing autogenous healing capacity of cementitious composites under cracking and healing cycles in aggressive waters, Construct. Build. Mater. 266 (2021), 121447.
[64] T. Fu, F. Montes, P. Suraneni, J. Youngblood, J. Weiss, The influence of cellulose nanocrystals on the hydration and flexural strength of Portland cement pastes, Polymers 9 (9) (2017) 424.
[65] E. Cuenca, V. Postolachi, L. Ferrara, Cellulose nanofibers to improve the mechanical and durability performance of self-healing Ultra-High Performance Concretes exposed to aggressive waters, Construct. Build. Mater. 374 (2023), 130785.
[66] F. Montes, T. Fu, J.P. Youngblood, J. Weiss, Rheological impact of using cellulose nanocrystals (CNC) in cement pastes, Construct. Build. Mater. 235 (2020), 117497.
[67] S. Nassiri, Z. Chen, G. Jian, T. Zhong, M.M. Haider, H. Li, C. Fernandez, M. Sinclair, T. Varga, L.S. Fifield, Comparison of unique effects of two contrasting types of cellulose nanomaterials on setting time, rheology, and compressive strength of cement paste, Cement Concr. Compos. 123 (2021), 104201.
[68] J. Flores, M. Kamali, A. Ghahremaninezhad, An investigation into the properties and microstructure of cement mixtures modified with cellulose nanocrystal, Materials 10 (5) (2017) 498.
[69] Q. Liu, Y. Peng, L. Liang, X. Dong, H. Li, Effect of cellulose nanocrystals on the properties of cement paste, J. Nanomater. (2019) 2019.
[70] D. Zheng, H. Yang, W. Feng, Y. Fang, H. Cui, Modification mechanism of cellulose nanocrystals in cement, Cement Concr. Res. 165 (2023), 107089.
[71] A. Picker, L. Nicoleau, Z. Burghard, J. Bill, I. Zlotnikov, C. Labbez, A. Nonat, H. Cölfen, Mesocrystalline calcium silicate hydrate: a bioinspired route toward elastic concrete materials, Sci. Adv. 3 (11) (2017), e1701216.
[72] J. Li, W. Zhang, K. Xu, P.J. Monteiro, Fibrillar calcium silicate hydrate seeds from hydrated tricalcium silicate lower cement demand, Cement Concr. Res. 137 (2020), 106195.
[73] S. Bhattacharjee, DLS and zeta potential–what they are and what they are not? J. Contr. Release 235 (2016) 337–351.
[74] M. Korayem, M. Taheri, Modeling of various contact theories for the manipulation of different biological micro/nanoparticles based on AFM, J. Nanoparticle Res. 16 (1) (2014) 1–18.
[75] H. Zhao, Y. Yue, L. Guo, J. Wu, Y. Zhang, X. Li, S. Mao, X. Han, Cloning nacre's 3D interlocking skeleton in engineering composites to achieve exceptional mechanical properties, Adv. Mater. 28 (25) (2016) 5099–5105.
[76] S. Naduparambath, T. Jinitha, V. Shaniba, M. Sreejith, A.K. Balan, E. Purushothaman, Isolation and characterisation of cellulose nanocrystals from sago seed shells, Carbohydr. Polym. 180 (2018) 13–20.
[77] A. Picker, L. Nicoleau, A. Nonat, C. Labbez, H. Cölfen, Identification of binding peptides on calcium silicate hydrate: a novel view on cement additives, Adv. Mater. 26 (7) (2014) 1135–1140.
[78] X. Ouyang, D. Koleva, G. Ye, K. Van Breugel, Understanding the adhesion mechanisms between CSH and fillers, Cement Concr. Res. 100 (2017) 275–283.
[79] K.A.S. Usman, C.J.O. Bacal, J. Zhang, S. Qin, P.A. Lynch, P. Mota-Santiago, M. Naebe, L.C. Henderson, D.Y. Hegh, J.M. Razal, Tough and fatigue resistant cellulose nanocrystal stitched $Ti_3C_2T_x$ MXene Films, Macromol. Rapid Commun. 43 (11) (2022), 2200114.
[80] M. Delhorme, C. Labbez, M. Turesson, E. Lesniewska, C.E. Woodward, B. Jönsson, Aggregation of calcium silicate hydrate nanoplatelets, Langmuir 32 (8) (2016) 2058–2066.
[81] K. Liu, X. Cheng, Y. Ma, X. Gao, C. Zhang, Z. Li, J. Zhuang, Analysis of interfacial nanostructure and interaction mechanisms between cellulose fibres and calcium silicate hydrates using experimental and molecular dynamics simulation data, Appl. Surf. Sci. 506 (2020), 144914.
[82] Z. Tang, N.A. Kotov, S. Magonov, B. Ozturk, Nanostructured artificial nacre, Nat. Mater. 2 (6) (2003) 413–418.
[83] F. Pelisser, P. Gleize, A. Mikowski, Effect of poly (diallyldimethylammonium chloride) on nanostructure and mechanical properties of calcium silicate hydrate, Mater. Sci. Eng., A 527 (26) (2010) 7045–7049.
[84] J. George, R. Kumar, V.A. Sajeevkumar, K.V. Ramana, R. Rajamanickam, V. Abhishek, S. Nadanasabapathy, Hybrid HPMC nanocomposites containing bacterial cellulose nanocrystals and silver nanoparticles, Carbohydr. Polym. 105 (2014) 285–292.
[85] S. Song, S. Qiang, J. Liang, L. Li, Y. Shi, J. Nie, T. Chen, S. Yao, M. Zhang, Cellulose nanofibril/mineral composites induced by H-bond/ionic coordination in co-refining system, Carbohydr. Polym. 289 (2022), 119425.
[86] F. Doustdar, A. Olad, M. Ghorbani, Effect of glutaraldehyde and calcium chloride as different crosslinking agents on the characteristics of chitosan/cellulose nanocrystals scaffold, Int. J. Biol. Macromol. 208 (2022) 912–924.
[87] H. Li, Y. Liu, K. Yang, C. Liu, X. Guan, S. Liu, G. Jing, Effects of synthetic CSH-tartaric acid nanocomposites on the properties of ordinary Portland cement, Cement Concr. Compos. 129 (2022), 104466.
[88] X. Liu, P. Feng, X. Yu, X. Shen, G. Geng, B. Lothenbach, The physiochemical alterations of calcium silicate hydrate (CSH) under magnesium attack, Cement Concr. Res. 160 (2022), 106901.
[89] G. Kim, S. Im, H. Jee, H. Suh, S. Cho, M. Kanematsu, S. Morooka, T. Koyama, Y. Nishio, A. Machida, Effect of magnesium silicate hydrate (MSH) formation on the local atomic arrangements and mechanical properties of calcium silicate hydrate (CSH): in situ X-ray scattering study, Cement Concr. Res. 159 (2022), 106869.
[90] Z.H. Feizi, P. Fatehi, Changes in the molecular structure of cellulose nanocrystals upon treatment with solvents, Cellulose 28 (11) (2021) 7007–7020.
[91] H. Zhuo, Y. Hu, Z. Chen, X. Peng, H. Lai, L. Liu, Q. Liu, C. Liu, L. Zhong, Linking renewable cellulose nanocrystal into lightweight and highly elastic carbon aerogel, ACS Sustain. Chem. Eng. 8 (32) (2020) 11921–11929.
[92] X. Zhu, C. Qian, B. He, Q. Chen, Z. Jiang, Experimental study on the stability of CSH nanostructures with varying bulk CaO/SiO_2 ratios under cryogenic attack, Cement Concr. Res. 135 (2020), 106114.
[93] R. Maddalena, K. Li, P. A.Chater, S. Michalik, A. Hamilton, Direct synthesis of a solid calcium-silicate-hydrate (CSH), Construct, Build. Mater. 223 (2019) 554–565.
[94] M. Vandamme, F.-J. Ulm, Nanoindentation investigation of creep properties of calcium silicate hydrates, Cement Concr. Res. 52 (2013) 38–52.
[95] J.J. Kim, E.M. Foley, M.M.R. Taha, Nano-mechanical characterization of synthetic calcium–silicate–hydrate (C–S–H) with varying CaO/SiO_2 mixture ratios, Cement Concr. Compos. 36 (2013) 65–70.
[96] Z. Hu, M. Wyrzykowski, M. Griffa, K. Scrivener, P. Lura, Young's modulus and creep of calcium-silicate-hydrate compacts measured by microindentation, Cement Concr. Res. 134 (2020), 106104.
[97] Y. Wang, R. Xie, D. Li, Y. Shen, W. Xie, H. Wang, L. Gan, J. Huang, A cross-linking/percolating-integrated strategy to enhance crystallizable rubber using rod-like reactive biobased nanocrystals, ACS Appl. Bio Mater. 3 (1) (2019) 441–449.
[98] M. Mariano, N. El Kissi, A. Dufresne, Cellulose nanocrystals and related nanocomposites: review of some properties and challenges, J. Polym. Sci. B Polym. Phys. 52 (12) (2014) 791–806.
[99] J. Yin, W. Li, J. Wang, X. Kong, Irreversible microstructural changes of calcium silicate hydrate during the first drying-resaturation cycle, Cement Concr. Res. 163 (2023), 107032.
[100] N. Grishkewich, N. Mohammed, J. Tang, K.C. Tam, Recent advances in the application of cellulose nanocrystals, Curr. Opin. Colloid Interface Sci. 29 (2017) 32–45.